Original Article

Development and validation of a multivariable risk model based on clinicopathological characteristics, mammography, and MRI imaging features for predicting axillary lymph node metastasis in patients with upgraded ductal carcinoma *in situ*

Min-Yi Cheng[1#]^, Can-Gui Wu[1#], Ying-Yi Lin[2#], Jia-Chen Zou[1], Dong-Qing Wang[1], Bruce G. Haffty[3], Kun Wang[1,2]^

[1]Department of Breast Cancer, Cancer Center, Guangdong Provincial People's Hospital (Guangdong Academy of Medical Sciences), Southern Medical University, Guangzhou, China; [2]School of Medicine, South China University of Technology, Guangzhou, China; [3]Department of Radiation Oncology, Robert Wood Johnson Medical School, Rutgers Cancer Institute, New Brunswick, NJ, USA

Contributions: (I) Conception and design: MY Cheng; (II) Administrative support: K Wang; (III) Provision of study materials or patients: K Wang; (IV) Collection and assembly of data: CG Wu, YY Lin; (V) Data analysis and interpretation: DQ Wang; (VI) Manuscript writing: All authors; (VII) Final approval of manuscript: All authors.

[#]These authors contributed equally to this work.

Correspondence to: Kun Wang, MD, PhD. Department of Breast Cancer, Cancer Center, Guangdong Provincial People's Hospital (Guangdong Academy of Medical Sciences), Southern Medical University, Zhongshan ER Road, Guangzhou 510080, China; School of Medicine, South China University of Technology, Guangzhou, China. Email: wangkun@gdph.org.cn.

Background: Axillary surgical staging is required for patients with upgraded ductal carcinoma in situ (DCIS) (DCIS is diagnosed on core biopsy with invasive cancer found on pathology after complete surgical excision), which may lead to complications in axillary surgery. At present, there is no reliable and accurate method for predicting axillary lymph node metastasis (ALNM) in patients with upgraded DCIS; however, such a method could prevent unnecessary axillary surgical interventions from being performed. In this study, we aimed to construct a non-invasive model for predicting ALNM in DCIS patients based on clinicopathological characteristics, mammography (MG) features, and magnetic resonance imaging (MRI) features.

Methods: Between February 2018 and June 2020, 326 patients with upgraded DCIS were enrolled in this retrospective analysis. These patients were randomly divided into the training cohort (80%) and validation cohort (20%). Univariate and multivariable regression analyses were conducted to identify the candidate pathological features, which then used to develop a clinicopathological model. The features of the 2-mm, 4-mm, and 6-mm intratumoral and peritumoral regions (T-PTR) were extracted to develop the MRI radiomics model, and two deep learning classification models were developed based on the medial-lateral oblique (MLO) and craniocaudal (CC) views of the MG. A fusion model was then established that combined these sub-models. The receiver operating characteristic (ROC) curve, area under the curve (AUC), and other indicators were used to evaluate the performance of these models.

Results: The clinicopathological characteristics of the two cohorts were basically balanced. The AUC values of the clinicopathological model were 0.675 and 0.690 in the training and validation cohorts, respectively. The model based on the T-PTR of MRI showed promising predictive ability. Among the three MRI models, the T-PTR (4 mm) model showed the best predictivity both in the training (AUC =0.885) and validation cohorts (AUC =0.843). The AUC values for the deep learning models of the MG CC and MLO positions all exceeded 0.7, indicating reliable predictive performance. The fusion model that combined the three methods significantly improved the accuracy and robustness of ALNM prediction. In both the training

^ ORCID: Min-Yi Cheng, 0000-0003-1140-3713; Kun Wang, 0000-0001-9851-7080.

(AUC =0.975) and validation (AUC =0.877) cohorts, the fusion model showed excellent performance.

Conclusions: We developed a fusion model that combined clinicopathological characteristics, MRI T-PTR (4 mm) radiomics, and MG-based deep learning. Our combined model showed promising performance in predicting ALNM in patients with upgraded DCIS.

Keywords: Breast cancer (BC); ductal carcinoma in situ (DCIS); mammography (MG); axillary lymph node metastasis (ALNM); magnetic resonance imaging (MRI)

Submitted Feb 27, 2025. Accepted for publication Apr 02, 2025. Published online Apr 25, 2025.
doi: 10.21037/gs-2025-89
View this article at: https://dx.doi.org/10.21037/gs-2025-89

Introduction

Approximately 30% of newly diagnosed breast cancer (BC) lesions are classified as ductal carcinoma in situ (DCIS) (1). A lesion is classified as upgraded DCIS if a non-invasive component is detected in the preoperative biopsy, but invasive ductal carcinoma is only found on pathology after complete surgical excision. Previous studies have reported that the underestimation risks of DCIS range from 14% to 43% (2,3), while one meta-analysis estimated the risk of upgraded DCIS to be 25.9% (4). The patients with upgraded DCIS may need to undergo a conventional sentinel lymph node biopsy (SLNB) (5,6). However, such patients face logistical and emotional challenges related to the need for additional axillary surgery and possible complications related to axillary surgery, such as pain, numbness, and arm swelling.

The overtreatment (unnecessary axillary surgery, including SLNB) could be avoided by predicting the likelihood of axillary lymph node metastasis (ALNM) in patients with upgraded DCIS pre-surgery. Many researchers have attempted to identify different factors or biomarkers to predict upgraded DCIS; for example, immunohistochemical biomarkers and imaging examination findings have been reported to be related to the prognosis of DCIS patients (4,7-12). However, these factors cannot serve as clear and reliable predictive factors for clinical decision making.

Recently, with the gradual integration of artificial intelligence, radiomics has been attracting increasing attention from researchers (13). At present, radiomics methods are able to transform images into exploitable data using large-scale medical image features to fulfil specific clinical requirements. For DCIS, radiomics methods based on ultrasound (US), mammography (MG), and magnetic resonance imaging (MRI) (14-18) have been applied in predicting ALNM. MRI and MG have advantages in predicting ALNM because of their relative objectivity and the low cost. MG is a common method used in the detection and diagnosis of BC. MG has good sensitivity in detecting calcification in MG images, while MRI has good specificity and sensitivity in detecting tumor lesions (19). Radiomics models based on MG and MRI can detect ALNM effectively (20-26). Previous studies have all explored a single method. Thus, this study sought to build a model based on MG deep learning and MRI radiomics combined with clinicopathological characteristics to predict ALNM in patients with upgraded DCIS. We present this article in accordance with the TRIPOD reporting checklist (available at https://gs.amegroups.com/article/view/10.21037/gs-2025-89/rc).

Highlight box

Key findings

- We developed a fusion model that combined clinicopathological characteristics, magnetic resonance imaging (MRI) intratumoral and peritumoral region (4 mm) radiomics, and mammography (MG)-based deep learning that showed promising performance in predicting axillary lymph node metastasis (ALNM) in patients with upgraded ductal carcinoma in situ (DCIS).

What is known, and what is new?

- Previous studies have exclusively utilized single-method approaches (e.g., MG or MRI alone) to predict ALNM in breast cancer.
- This study introduces an innovative combined model integrating MG deep learning features, MRI radiomics, and clinicopathological characteristics. By leveraging multi-modal data fusion, the model achieves superior predictive efficacy for ALNM compared to conventional single-method strategies.

What is the implication, and what should change now?

- This non-invasive model showed good efficacy in predicting ALNM in patients with upgraded DCIS, and it can be used to avoid unnecessary axillary surgical intervention.

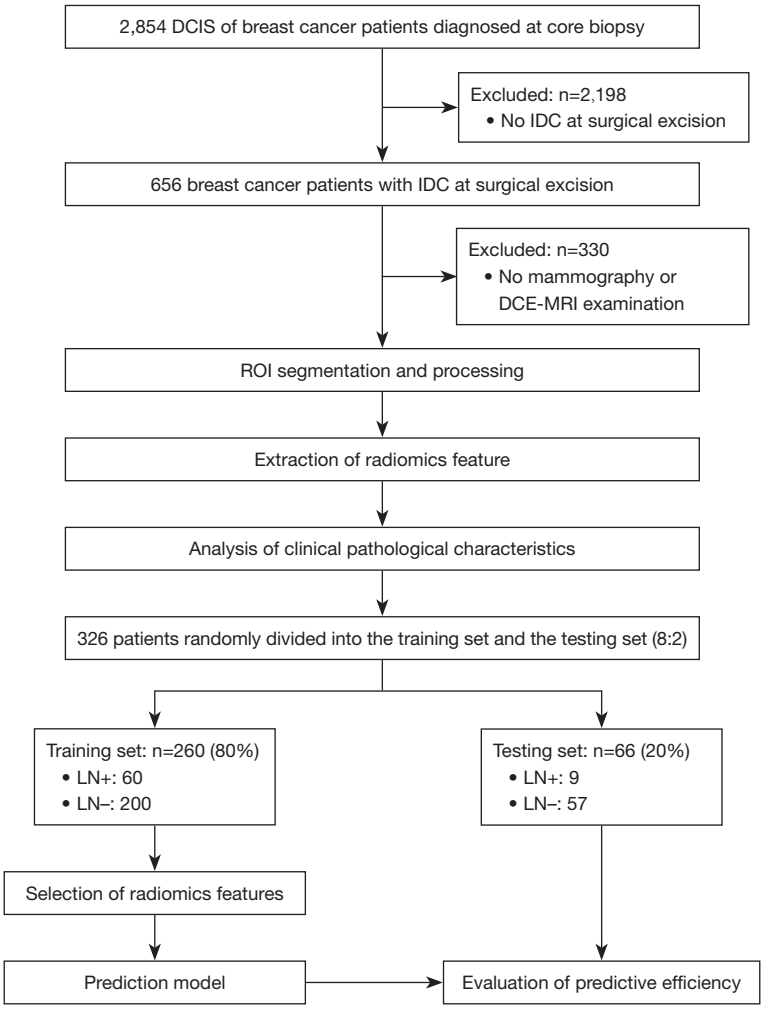

Figure 1 Workflow diagram showing the study's inclusion and exclusion criteria. DCE-MRI, dynamic contrast enhanced magnetic resonance imaging; DCIS, ductal carcinoma in situ; IDC, invasive ductal carcinoma; LN, lymph node; ROI, region of interest.

Methods

Patients and data collection

The Ethics Committee of the Guangdong Provincial People's Hospital approved this study (No. KY-Q-2022-452-01; date: December 6, 2022), and the requirement of informed consent was waived due to the retrospective nature of this study. The study was conducted in accordance with the Declaration of Helsinki and its subsequent amendments. Between February 2018, and June 2020, 326 patients with complete imaging clinicopathological data were enrolled in this study. The 326 patients were randomly divided into two cohorts using an 8:2 randomization method. To be eligible for inclusion in the study, the patients had to meet the following inclusion criteria: (I) have undergone preoperative contrast-enhanced MRI and MG before biopsy; (II) have biopsy-proven DCIS and pathologically diagnosed invasive ductal carcinoma; and (III) have been treated with breast surgery and have had their axillary lymph node (ALN) status assessed by SLNB or axillary lymph node dissection (ALND). Patients were excluded from the study if they met any of the following exclusion criteria: (I) had undergone biopsy or chemoradiotherapy prior to the MRI examination; (II) had poor-quality images; (III) had incomplete clinicopathological data; and/or (IV) had not undergone surgical treatment (*Figure 1*).

Univariate and multivariable regression analyses

The association between each feature and lymph node

metastasis (LNM) was assessed by univariate analysis. The multivariable logistic regression analysis included the variables that were found to be statistically significant in the univariate analysis. The results of the multivariate analysis were used to identify independent predictors, which were then used to construct further clinical models. All statistical analyses (univariate and multivariable regression) were conducted on the training dataset. The testing dataset was strictly held out and only used for final validation without any prior interaction with the model development process.

MRI imaging acquisition

The MRI examinations were performed on a 1.5 T or 3.0 T MRI scanner (Ingenia, Philips, the Netherlands). For the analysis, T1-weighted, T2-weighted, dynamic contrast-enhanced (DCE), and diffusion-weighted images were acquired before the biopsy.

MG acquisition and preprocessing

Breast tomosynthesis was performed on a full-field digital MG system (Hologic, Marlborough, MA, USA). The imaging procedure included standard craniocaudal (CC) and medio-lateral oblique (MLO) views. The images were acquired using low-dose X-rays; the typical radiation dose ranged from 1 to 2 mGy. For the image analysis, calcifications, masses, and other lesions were carefully assessed and classified using the Breast Imaging-Reporting and Data System (BI-RADS). The radiologists extracted the region of interest (ROI) by manual freehand declination, using Labelme software (version 4.5.9, https://labelm.com/) in the CC and MLO views. The ROI included suspected calcification, mass, and other lesions (*Figure 2*).

Tumor lesion segmentation

MRI

The lesions were segmented in three dimensions using ITK-SNAP software (version 3.8, http://www.itksnap.org). The segmentation was conducted exclusively in the key enhancement phase of the DCE-sequenced MRI, and no other sequences were included in the segmentation process. Subsequently, peritumoral expansions (2 mm, 4 mm, and 6 mm) were automatically generated by Python software (version 3.9.0, https://www.python.org/) for further analysis and feature extraction. For patients with unilateral multifocal or multicentric lesions, only the largest tumor lesion was segmented and analyzed.

MG

In the mammographic images, tumor segmentation was carried out using the Labelme software (version 4.5.9). Standard MLO and CC breast images were selected, and the lesion area was manually labelled in each view. Rectangular contours were used for the segmentation to ensure the inclusion of the entire tumor and the surrounding tissue for subsequent analysis. In cases of multifocal or multicentric lesions, only the largest tumor lesion was segmented.

The segmentation of the MRI and MG images was conducted by an experienced radiologist (Y.C.), and subsequently reviewed by another senior radiologist (W.L.) to ensure the consistency and accuracy of the annotation. Two radiologists independently segmented ROIs in 40 randomly selected cases (12% of the dataset). Intraclass correlation coefficients (ICCs) were calculated for shape and texture features, with ICC >0.75 indicating good reproducibility. One radiologist repeated ROI segmentation after a 2-week interval, with ICCs calculated similarly.

Construction of intratumoral and peritumoral radiomics model using MRI radiomics

The Pyradiomics package of Python software (version 3.8) was employed to extract the radiomic features from the intratumoral and peritumoral regions (T-PTR) (2 mm, 4 mm, and 6 mm), enabling the construction of three models: T-PTR (2 mm), T-PTR (4 mm), and T-PTR (6 mm), adhering to the Image Biomarker Standardisation Initiative (IBSI) guidelines. The extracted features included the shape, texture, and first-order statistical features. Preprocessing steps involved resampling to 1 mm^3 isotropic resolution, intensity discretization (bin width =25 HU), and manual segmentation of regions of interest. The statistically significant features were first identified using the Mann-Whitney *U* test ($P<0.05$), and the Spearman rank correlation coefficient was then used to select the features with the highest correlations. Subsequently, a greedy recursive deletion strategy was employed to iteratively remove the most redundant features. Finally, to further optimize the feature subset, the maximum relevance minimum redundancy algorithm was used to eliminate any redundant features, and only those highly correlated with the classification labels were retained for

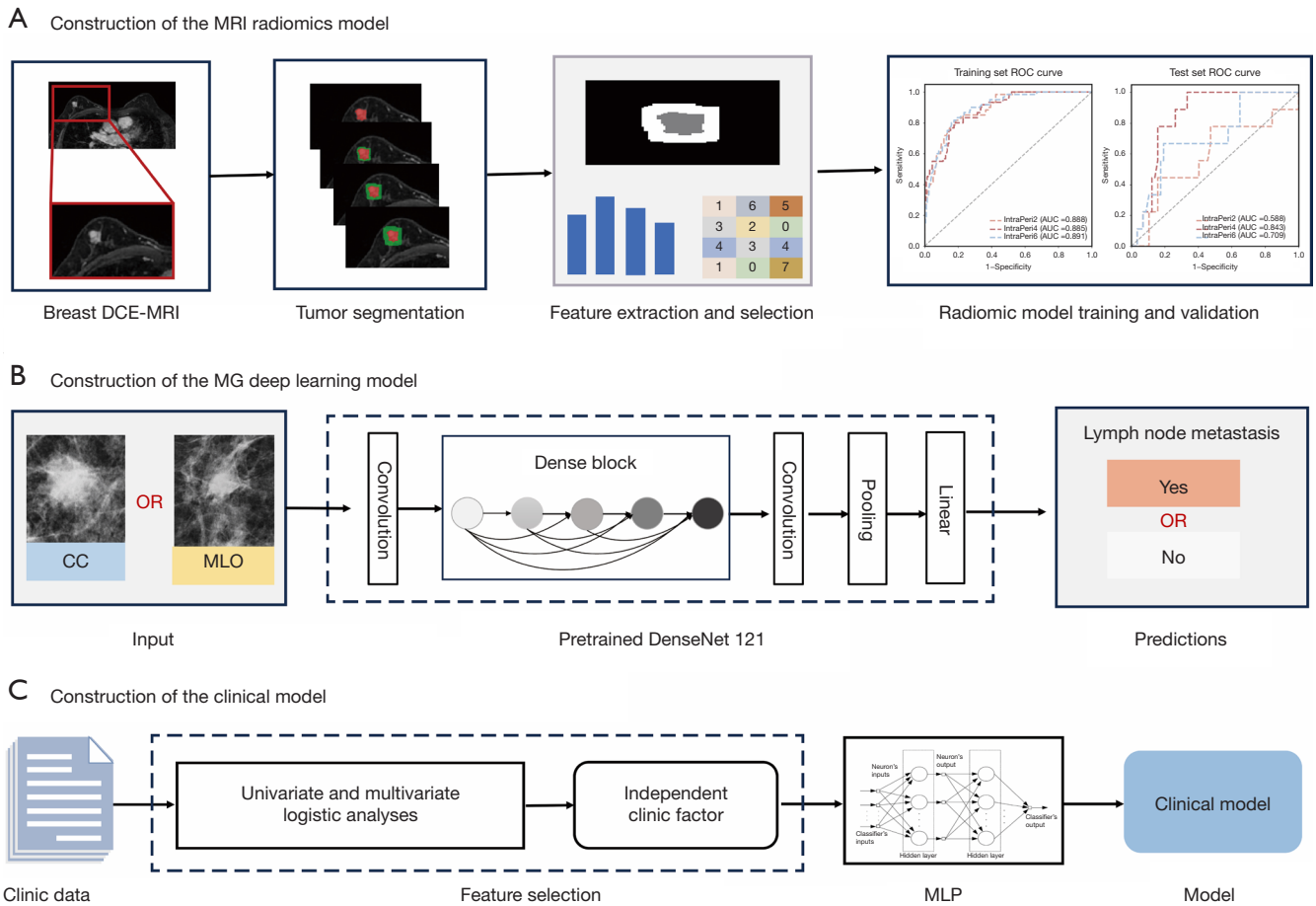

Figure 2 The flowchart of this study. This was a retrospective study with patients enrolled from our institution. MG, MRI and baseline data were collected. A total of 326 patients were randomly divided into the training cohort (80%) and validation cohort (20%). (A) Construction of the MRI radiomics model. (B) Construction of the MG deep learning model. (C) Construction of the clinical model. We developed a fusion model that combined clinicopathological characteristics, MRI radiomics, and MG-based deep learning. CC, craniocaudal; DCE-MRI, dynamic contrast enhanced magnetic resonance imaging; MG, mammography; MLO, medio-lateral oblique; MLP, multi-layer perceptron; MRI, magnetic resonance imaging.

model construction. T-PTR size selection was performed exclusively on the training dataset using 5-fold cross-validation. The 4-mm T-PTR was chosen based on the highest mean area under the curve (AUC) (0.885±0.03) across folds. The testing dataset was strictly held out and only used for final validation of the fusion model. Hyperparameters for the support vector machine (SVM) fusion model were optimized via grid search on the training dataset's cross-validation folds.

MG deep learning model construction

In our study, we constructed two deep learning classification models based on the MLO and CC views of the breast mammograms, respectively. The models employed transfer learning. The DenseNet201 network pre-trained on the ImageNet (https://image-net.org/) dataset was used for the image feature extraction and classification, and fine-tuned to meet the specific requirements of mammogram classification. The dataset was then divided and trained using a five-fold cross-validation strategy. Key hyperparameters included an initial learning rate of 0.01, a batch size of 32, and 50 training epochs. The training process used stochastic gradient descent (SGD) as the optimizer, and ImageNet normalization was applied

during data preprocessing to enhance the effectiveness of the transfer learning. The training process used a single graphics processing unit for computational efficiency. Cross-entropy loss was selected as the loss function, and early stopping was implemented to monitor validation set performance and prevent overfitting. Each image sample was normalized to meet the input specifications of the DenseNet201 model. Ultimately, two classification models based on the MLO and CC MG views were constructed and optimized to predict the ALN status of the BC patients. The DenseNet201 models for MLO and CC views were trained exclusively on the training dataset. A five-fold cross-validation strategy was applied to the training data for hyperparameter tuning, with early stopping based on validation loss from the cross-validation folds. The held-out validation/testing dataset remained entirely unseen during training. Data preprocessing parameters were computed from the training dataset alone. Training used SGD with learning rate decay, batch size 32, and ImageNet-based initialization.

Fusion model construction and evaluation

This study integrated the results of multiple sub-models to construct a fusion model that could more accurately predict breast lesions. The fusion model combined the predictive probabilities of three independent sub-models, including a clinical model, an optimal MRI intratumoral and peritumoral radiomics model, and a MG (CC + MLO) deep learning model. To achieve more effective results, we employed a SVM approach to establish the post-fusion model. Initially, each of the three sub-models was independently trained to generate predictive probabilities for breast lesions. These probabilities were then used as input features for the SVM model. To address the nonlinear relationships between predictions from the different sub-models, the SVM used a radial basis function as its kernel function. Additionally, the selection of hyperparameters was optimized through cross-validation and grid search to ensure robust generalization and superior predictive performance.

Statistical analysis

R software (version 3.5.0, https://www.r-project.org/) and Python (version 3.9.0) were used for the statistical analysis in this study. The continuous variables are expressed as the mean ± standard deviation, or the median (interquartile range), while the categorical variables are presented as the frequency and percentage. The Mann-Whitney *U* test or the independent *t*-test was used to compare the continuous variables between groups, while the chi-square test or Fisher's exact test was used to compare the categorical variables. A P value <0.05 was considered statistically significant. The Mann-Whitney *U* test, Chi-square test, or Fisher's exact test was used to assess the association of each clinical feature with the clinical outcomes in the univariate analysis. The performance of the predictive models was evaluated using the receiver operating characteristic (ROC) curve and the AUC, along with other indicators for comprehensive assessment.

Results

Patient characteristics

The mean age of the 326 patients enrolled in the study was 49.5±10.7 years (range, 28 to 72 years). Of the patients, 69 (21.2%) were diagnosed with pathological ALNM, while the 297 had pathologically negative axillary nodes (pN0). The training cohort comprised 260 patients (60 ALNM patients; range, 31–68 years), and the validation cohort comprised 66 patients (9 ALNM patients; range, 28–72 years). Of the 326 patients, 269 (82.5%) underwent SLNB alone, 18 (5.52%) underwent ALND alone, and 39 (12.0%) underwent SLNB followed by ALND. The results of our comparison of the MRI, MG, and clinicopathological characteristics between our training and validation cohorts are shown in *Table 1*. Notably, no statistically significant differences were observed between the variables in the two cohorts (*Tables 1*,*2*).

Univariate and multivariate analyses of ALN

The univariate analysis showed that the patients with lower density breast glandular tissue were more likely to develop LNMs after glandular atrophy (P<0.05) (*Table 2*). Moreover, the results of the multivariate analysis revealed that a younger age was significantly associated with a higher risk of ALNM in the training cohort (P=0.006). Both the univariate and multivariate analyses revealed that the occurrence of LNM was higher in the patients with a mass on MG, and a higher BI-RADS grade on breast MRI (all P<0.05). Additionally, the hormone receptor (HR)-positive [estrogen receptor (ER)] patients had a significantly higher probability of ALNM (P<0.05). Based on these findings, age, ER status, mammographic abnormalities, MG mass

Table 1 Clinical and pathological characteristics of the patients in the training and testing sets

Characteristics	All patients (n=326)	Testing set (n=66)	Training set (n=260)	P
Age (years)	49.5±10.7	49.2±11.4	49.6±10.5	0.78
MG abnormalities				0.32
Calcification	88 (27.0)	17 (25.8)	71 (27.3)	
Mass	58 (17.8)	13 (19.7)	45 (17.3)	
Mass and calcification	128 (39.3)	25 (37.9)	103 (39.6)	
No abnormalities	33 (10.1)	4 (6.06)	29 (11.2)	
Structural distortion asymmetry	19 (5.83)	7 (10.6)	12 (4.62)	
Palpable				>0.99
No	34 (10.4)	7 (10.6)	27 (10.4)	
Yes	292 (89.6)	59 (89.4)	233 (89.6)	
MG visible				>0.99
No	42 (12.9)	9 (13.6)	33 (12.7)	
Yes	284 (87.1)	57 (86.4)	227 (87.3)	
MG density				>0.99
0–50%	222 (68.1)	45 (68.2)	177 (68.1)	
50–100%	104 (31.9)	21 (31.8)	83 (31.9)	
MG maximum diameter (cm)	3.05±2.19	2.95±1.94	3.08±2.26	0.65
MG size level				0.38
0	35 (10.7)	4 (6.06)	31 (11.9)	
1	67 (20.6)	15 (22.7)	52 (20.0)	
2	224 (68.7)	47 (71.2)	177 (68.1)	
MG BI-RADS				0.40
0	12 (3.68)	4 (6.06)	8 (3.08)	
1	1 (0.31)	0 (0.00)	1 (0.38)	
2	12 (3.68)	2 (3.03)	10 (3.85)	
3	26 (7.98)	2 (3.03)	24 (9.23)	
4	154 (47.2)	35 (53.0)	119 (45.8)	
5	121 (37.1)	23 (34.8)	98 (37.7)	
MG characteristics				0.38
No calcification	115 (35.3)	26 (39.4)	89 (34.2)	
Clusters, line, or segment distribution	153 (46.9)	32 (48.5)	121 (46.5)	
Density and morphological heterogeneous	58 (17.8)	8 (12.1)	50 (19.2)	
MG calcification morphology				0.09
No calcification	115 (35.3)	26 (39.4)	89 (34.2)	
Segment distribution	151 (46.3)	34 (51.5)	117 (45.0)	
Diffusion distribution	60 (18.4)	6 (9.09)	54 (20.8)	

Table 1 (*continued*)

Table 1 (*continued*)

Characteristics	All patients (n=326)	Testing set (n=66)	Training set (n=260)	P
MRI enhancement				0.70
No abnormalities	8 (2.45)	1 (1.52)	7 (2.69)	
Non-mass enhancement	75 (23.0)	17 (25.8)	58 (22.3)	
Mass enhancement	240 (73.6)	47 (71.2)	193 (74.2)	
Asymmetric enhancement	3 (0.92)	1 (1.52)	2 (0.77)	
MRI visible				>0.99
No	8 (2.45)	1 (1.52)	7 (2.69)	
Yes	318 (97.5)	65 (98.5)	253 (97.3)	
MRI maximum diameter (cm)	3.13±1.82	2.91±1.45	3.19±1.90	0.20
MRI BI-RADS				0.85
1	4 (1.23)	1 (1.52)	3 (1.15)	
2	1 (0.31)	0 (0.00)	1 (0.38)	
3	11 (3.37)	3 (4.55)	8 (3.08)	
4	170 (52.1)	35 (53.0)	135 (51.9)	
5	140 (42.9)	27 (40.9)	113 (43.5)	
Lesion location				>0.99
Left	177 (54.3)	36 (54.5)	141 (54.2)	
Right	149 (45.7)	30 (45.5)	119 (45.8)	
Biopsy pathology				0.45
Low-grade DCIS	9 (2.76)	1 (1.52)	8 (3.08)	
Mid-grade DCIS	93 (28.5)	15 (22.7)	78 (30.0)	
high-grade DCIS	224 (68.7)	50 (75.8)	174 (66.9)	
IDC grade				0.55
I	30 (9.20)	8 (12.1)	22 (8.46)	
II	184 (56.4)	38 (57.6)	146 (56.2)	
III	112 (34.4)	20 (30.3)	92 (35.4)	
Breast surgery				>0.99
Mastectomy	300 (92.0)	61 (92.4)	239 (91.9)	
BCS	26 (7.98)	5 (7.58)	21 (8.08)	
Axillary surgery				0.13
SLNB	269 (82.5)	60 (90.9)	209 (80.4)	
SLNB + ALND	18 (5.52)	1 (1.52)	17 (6.54)	
ALND	39 (12.0)	5 (7.58)	34 (13.1)	
ER				0.41
Negative	107 (32.8)	25 (37.9)	82 (31.5)	
Positive	219 (67.2)	41 (62.1)	178 (68.5)	

Table 1 (*continued*)

Table 1 (*continued*)

Characteristics	All patients (n=326)	Testing set (n=66)	Training set (n=260)	P
PR				0.22
Negative	134 (41.1)	32 (48.5)	102 (39.2)	
Positive	192 (58.9)	34 (51.5)	158 (60.8)	
HER2				0.84
Negative	169 (51.8)	33 (50.0)	136 (52.3)	
Positive	157 (48.2)	33 (50.0)	124 (47.7)	
Ki67 (%)	27±20	27±21	27±20	0.92
pT				0.93
1	147 (45.1)	31 (47.0)	116 (44.6)	
2	169 (51.8)	33 (50.0)	136 (52.3)	
3	10 (3.07)	2 (3.03)	8 (3.08)	

The continuous variables are presented as mean ± standard deviation and the categorical variables are presented as the frequency and percentage. ALND, axillary lymph node dissection; BCS, breast conserving surgery; BI-RADS, Breast Imaging-Reporting and Data System; DCIS, ductal carcinoma *in situ*; ER, estrogen receptor; HER2, human epidermal growth factor receptor 2; IDC, infiltrating ductal carcinoma; MG, mammography; MRI, magnetic resonance imaging; PR, progesterone receptor; SLNB, sentinel lymph node biopsy.

size, and MRI BI-RADS classification were identified as independent predictors of LNM and were incorporated into the construction of the clinical model (*Figure 1*).

Model performance evaluation

Clinical model

The results indicated that the clinical model had stable predictive ability in both the training (AUC =0.675) and validation (AUC =0.690) cohorts (*Table 3*, *Figure 3*), and thus could serve as the baseline control model.

Intratumoral and peritumoral radiomics model based on MRI

The radiomics model based on T-PTR of MRI showed strong predictive performance. In the training cohort, the AUC values for the different expansion areas were as follows: T-PTR (2 mm) model: 0.888; T-PTR (4 mm) model: 0.885, and T-PTR (6 mm) model: 0.891. All the AUCs indicated that the models had high predictive accuracy. Correspondingly, in the validation set, the AUC values were 0.588, 0.843, and 0.709, respectively. Notably, the T-PTR (4 mm) model exhibited the best efficacy in the validation cohort, demonstrating superior generalization ability. Therefore, the T-PTR (4 mm) model was selected for the further construction of the subsequent model (*Table 3*, *Figure 3*).

MG deep learning model

In the training set, the AUC values were 0.784 and 0.896 for the deep learning models of the MG CC and MLO views, respectively. In the testing set, the performance of this model was reliable, with the MLO position (AUC =0.790) performing slightly better than the CC position (AUC =0.737) (*Table 3*, *Figure 3*). These results showed the potential of molybdenum target images in predicting LNM.

Fusion model

Using the SVM for the post-fusion of various sub-models, the fusion model had an AUC value of 0.975 in the training set, and an AUC value of 0.877 in the validation set, both of which were significantly better than those of the sub-models. This indicated that the fusion model could effectively integrate multi-source information, significantly enhancing the accuracy and robustness of breast lesion prediction (*Table 3*, *Figure 3*).

Discussion

In this study, we conducted a multivariate analysis and integrated the clinicopathological characteristics with MRI radiomics and MG deep learning technologies to construct

Table 2 Clinicopathologic characteristics and breast tumor descriptors based on MRI and MG of all patients in non-mALN and mALN groups from the two datasets

Items	Training set					Testing set			
	All (n=260)	Non-mALN (n=200)	mALN (n=60)	Univariate P	Multivariate P	All (n=66)	Non-mALN (n=57)	mALN (n=9)	P
Age (years)	49.59±10.49	50.11±10.70	47.85±9.65	0.27	0.006	49.15±11.43	50.49±11.24	40.67±9.18	0.02
MG maximum diameter (cm)	3.08±2.26	2.90±2.14	3.66±2.54	0.10	0.02	2.95±1.94	2.99±2.04	2.69±1.18	0.74
MRI maximum diameter (cm)	3.19±1.90	3.20±1.86	3.16±2.05	0.47	0.08	2.91±1.45	2.89±1.51	2.99±1.11	0.63
Ki67 (%)	26.78±20.09	26.43±20.22	27.93±19.80	0.56	0.19	26.47±21.29	25.21±22.13	34.44±13.10	0.041
MG abnormalities				0.001	0.01				0.72
Calcification	71 (27.31)	44 (22.00)	27 (45.00)			17 (25.76)	15 (26.32)	2 (22.22)	
Mass	45 (17.31)	35 (17.50)	10 (16.67)			13 (19.70)	11 (19.30)	2 (22.22)	
Mass and calcification	103 (39.62)	85 (42.50)	18 (30.00)			25 (37.88)	22 (38.60)	3 (33.33)	
No abnormalities	29 (11.15)	28 (14.00)	1 (1.67)			4 (6.06)	4 (7.02)	0	
Structural distortion asymmetry	12 (4.62)	8 (4.00)	4 (6.67)			7 (10.61)	5 (8.77)	2 (22.22)	
Palpable				0.40	0.67				>0.99
No	27 (10.38)	23 (11.50)	4 (6.67)			7 (10.61)	6 (10.53)	1 (11.11)	
Yes	233 (89.62)	177 (88.50)	56 (93.33)			59 (89.39)	51 (89.47)	8 (88.89)	
MG visible				0.07	0.44				>0.99
No	33 (12.69)	30 (15.00)	3 (5.00)			9 (13.64)	8 (14.04)	1 (11.11)	
Yes	227 (87.31)	170 (85.00)	57 (95.00)			57 (86.36)	49 (85.96)	8 (88.89)	
MG density				0.045	0.53				0.62
0–50%	177 (68.08)	143 (71.50)	34 (56.67)			45 (68.18)	40 (70.18)	5 (55.56)	
50–100%	83 (31.92)	57 (28.50)	26 (43.33)			21 (31.82)	17 (29.82)	4 (44.44)	
MG BI-RADS				0.78	0.96				0.23
0	8 (3.08)	7 (3.50)	1 (1.67)			4 (6.06)	4 (7.02)	0	
1	1 (0.38)	1 (0.50)	0			0 (0.00)	0	0	
2	10 (3.85)	9 (4.50)	1 (1.67)			2 (3.03)	1 (1.75)	1 (11.11)	
3	24 (9.23)	19 (9.50)	5 (8.33)			2 (3.03)	1 (1.75)	1 (11.11)	
4	119 (45.77)	92 (46.00)	27 (45.00)			35 (53.03)	30 (52.63)	5 (55.56)	
5	98 (37.69)	72 (36.00)	26 (43.33)			23 (34.85)	21 (36.84)	2 (22.22)	
MG calcification distribution				0.10	0.35				0.55
No calcification	89 (34.23)	73 (36.50)	16 (26.67)			26 (39.39)	21 (36.84)	5 (55.56)	
Clusters, line, or segment distribution	121 (46.54)	94 (47.00)	27 (45.00)			32 (48.48)	29 (50.88)	3 (33.33)	
Density and morphological heterogeneous	50 (19.23)	33 (16.50)	17 (28.33)			8 (12.12)	7 (12.28)	1 (11.11)	
MG calcification morphology				0.27	0.47				0.50
No calcification	89 (34.23)	73 (36.50)	16 (26.67)			26 (39.39)	21 (36.84)	5 (55.56)	
Segment distribution	117 (45.00)	89 (44.50)	28 (46.67)			34 (51.52)	31 (54.39)	3 (33.33)	
Diffusion distribution	54 (20.77)	38 (19.00)	16 (26.67)			6 (9.09)	5 (8.77)	1 (11.11)	
MRI enhancement				0.61	0.52				0.90
No abnormalities	7 (2.69)	6 (3.00)	1 (1.67)			1 (1.52)	1 (1.75)	0	
Non-mass enhancement	58 (22.31)	47 (23.50)	11 (18.33)			17 (25.76)	14 (24.56)	3 (33.33)	

Table 2 (*continued*)

Table 2 (*continued*)

Items	Training set					Testing set			
	All (n=260)	Non-mALN (n=200)	mALN (n=60)	Univariate P	Multivariate P	All (n=66)	Non-mALN (n=57)	mALN (n=9)	P
Mass enhancement	193 (74.23)	145 (72.50)	48 (80.00)			47 (71.21)	41 (71.93)	6 (66.67)	
Asymmetric enhancement	2 (0.77)	2 (1.00)	0			1 (1.52)	1 (1.75)	0	
MRI visible				0.92	0.67				>0.99
No	7 (2.69)	6 (3.00)	1 (1.67)			1 (1.52)	1 (1.75)	0	
Yes	253 (97.31)	194 (97.00)	59 (98.33)			65 (98.48)	56 (98.25)	9 (100.00)	
MRI BI-RADS				0.03	0.02				0.77
1	3 (1.15)	3 (1.50)	0			1 (1.52)	1 (1.75)	0	
2	1 (0.38)	1 (0.50)	0			0 (0.00)	0	0	
3	8 (3.08)	7 (3.50)	1 (1.67)			3 (4.55)	3 (5.26)	0	
4	135 (51.92)	113 (56.50)	22 (36.67)			35 (53.03)	29 (50.88)	6 (66.67)	
5	113 (43.46)	76 (38.00)	37 (61.67)			27 (40.91)	24 (42.11)	3 (33.33)	
Lesion location				0.07	0.42				0.77
Left	141 (54.23)	115 (57.50)	26 (43.33)			36 (54.55)	32 (56.14)	4 (44.44)	
Right	119 (45.77)	85 (42.50)	34 (56.67)			30 (45.45)	25 (43.86)	5 (55.56)	
Biopsy pathology				0.46	0.24				0.92
Low-grade DCIS	8 (3.08)	5 (2.50)	3 (5.00)			1 (1.52)	1 (1.75)	0	
Mid-grade DCIS	78 (30.00)	58 (29.00)	20 (33.33)			15 (22.73)	13 (22.81)	2 (22.22)	
High-grade DCIS	174 (66.92)	137 (68.50)	37 (61.67)			50 (75.76)	43 (75.44)	7 (77.78)	
IDC grade				0.74	0.85				0.83
I	22 (8.46)	18 (9.00)	4 (6.67)			8 (12.12)	7 (12.28)	1 (11.11)	
II	146 (56.15)	110 (55.00)	36 (60.00)			38 (57.58)	32 (56.14)	6 (66.67)	
III	92 (35.38)	72 (36.00)	20 (33.33)			20 (30.30)	18 (31.58)	2 (22.22)	
ER				<0.001	0.04				0.50
Negative	82 (31.54)	74 (37.00)	8 (13.33)			25 (37.88)	23 (40.35)	2 (22.22)	
Positive	178 (68.46)	126 (63.00)	52 (86.67)			41 (62.12)	34 (59.65)	7 (77.78)	
PR				0.03	0.31				0.18
Negative	102 (39.23)	86 (43.00)	16 (26.67)			32 (48.48)	30 (52.63)	2 (22.22)	
Positive	158 (60.77)	114 (57.00)	44 (73.33)			34 (51.52)	27 (47.37)	7 (77.78)	
HER2				0.07	0.07				>0.99
Negative	136 (52.31)	98 (49.00)	38 (63.33)			33 (50.00)	29 (50.88)	4 (44.44)	
Positive	124 (47.69)	102 (51.00)	22 (36.67)			33 (50.00)	28 (49.12)	5 (55.56)	
pT				0.16	0.64				0.52
1	116 (44.62)	92 (46.00)	24 (40.00)			31 (46.97)	28 (49.12)	3 (33.33)	
2	136 (52.31)	100 (50.00)	36 (60.00)			33 (50.00)	27 (47.37)	6 (66.67)	
3	8 (3.08)	8 (4.00)	0			2 (3.03)	2 (3.51)	0	

The continuous variables are presented as mean ± standard deviation and the categorical variables are presented as the frequency and percentage. BI-RADS, Breast Imaging-Reporting and Data System; DCIS, ductal carcinoma *in situ*; ER, estrogen receptor; HER2, human epidermal growth factor receptor 2; IDC, infiltrating ductal carcinoma; mALN, metastatic axillary lymph node; MG, mammography; MRI, magnetic resonance imaging; PR, progesterone receptor.

Table 3 Performance comparison of different models

Models	Training set				Testing set			
	Accuracy	AUC	Sensitivity	Specificity	Accuracy	AUC	Sensitivity	Specificity
Clinic	0.677	0.675	0.583	0.705	0.879	0.690	0.556	0.930
CCDTL	0.658	0.784	0.900	0.585	0.758	0.737	0.667	0.772
MLODTL	0.831	0.896	0.833	0.830	0.697	0.790	0.889	0.667
T-PTR (2 mm)	0.815	0.888	0.817	0.815	0.561	0.588	0.778	0.526
T-PTR (4 mm)	0.819	0.885	0.800	0.825	0.712	0.843	1.000	0.667
T-PTR (6 mm)	0.823	0.891	0.817	0.825	0.788	0.709	0.667	0.807
Fusion	0.935	0.975	0.917	0.940	0.727	0.877	1.000	0.684

AUC, area under the curve; CCDTL, mammography craniocaudal position deep learning model; Clinic, clinical model; MLODTL, mammography medial-lateral oblique position deep learning model; T-PTR, intratumoral and peritumoral region.

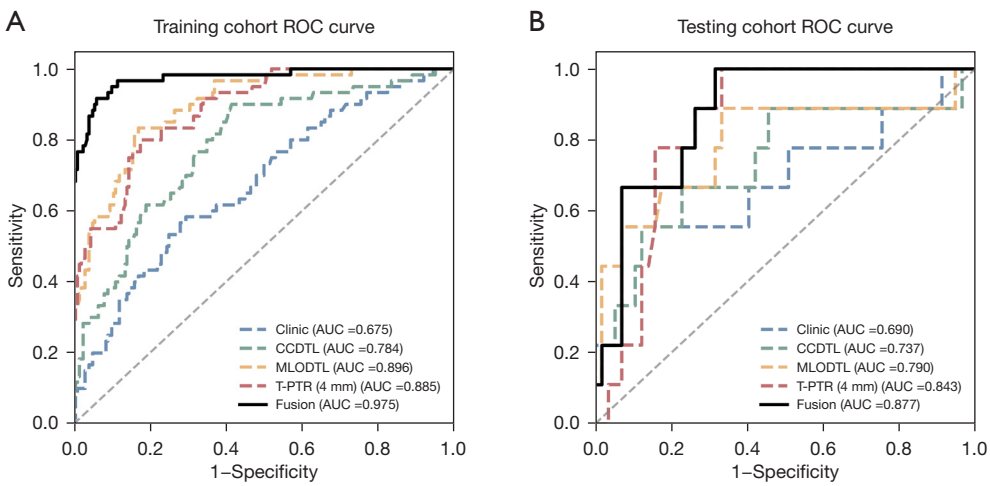

Figure 3 The ROC of the model from (A) the training cohort, (B) the testing cohort. AUC, area under the curve; CCDTL, mammography craniocaudal position deep learning model; Clinic, clinical model; MLODTL, mammography medial-lateral oblique position deep learning model; ROC, receiver operating characteristic; T-PTR, intratumoral and peritumoral region.

a prediction model for ALNM in patients with upgraded DCIS. The results showed that the combined model had better predictive power than the four sub-models, and achieved the highest AUC values in both the training (AUC =0.975) and validation sets (AUC =0.877). Our results showed that the fusion model effectively integrated multi-source information, and significantly improved the accuracy and robustness of ALNM prediction.

A previous study reported that age was also a risk factor for ALNM (27). Notably, the study reported that the risk of recurrence was higher in younger patients than older patients, and also reported a significant correlation between high grade tumors, lymphovascular invasion (LVI), and ALNM (27). The mean age of the BC patients enrolled in our study was 49.5 years at the time of diagnosis. We observed that age was an independent risk factor for predicting ALNM.

A previous study has not drawn conclusions on the role of ER and PR receptor status in predicting ALNM, and no association has been observed between HR status and lymph node positivity (28). However, recent studies have concluded that the risk of ALNM in HR negative patients was lower than that of other patients after adjusting for other risk factors (29-31). Interestingly, our study found a

significant correlation between ER status and ALNM, such that a higher proportion of the ALNM patients were ER-positive. These findings indicate that ER status could serve as an independent risk factor for ALNM.

Research has reported that the larger the tumor, the higher the likelihood of ALNM (32). However, small primary tumors have also been reported to show extensive LNM (33). Notably, our study found that tumor size was also an independent risk factor, such that the larger the maximum diameter of the MG lesion, the higher the risk of ALNM. Moreover, BI-RADS 5 lesions have been reported to be related to a larger tumor size, ALNM, and LVI on breast US examination. Similarly, our previous study showed that BI-RADS-MRI classification has important significance for predicting ALNM (34). In this study, the independent predictors of LNM included age, ER status, abnormal performance on MG, MG mass size, and BI-RADS-MRI classification.

MG radiography is widely used in BC screening and provides sufficient data for clinical diagnosis (24). In a study of 147 patients, a MG-based radiomics nomogram with some clinicopathologic features was developed to predict ALNM in BC patients, with greater than 0.8 AUC values (15). Moreover, another study established a combined radiomics nomogram to predict ALNM that included PR status, the subtype of BC, and the radiomics profile, and found that this combined nomogram was more effective than any one clinical or radiological feature alone (24). In our study, the AUC values of the MG deep learning prediction model for the CC view and MLO view in the training cohort were 0.784 and 0.896, respectively, and the corresponding AUC values for the training cohort were 0.737 and 0.790, respectively. Thus, the deep learning MG model also has potential clinical value in predicting LNM.

We found that the T-PTR (4 mm) model showed promising performance in predicting ALNM, and had AUC values greater than 0.8 in both the training and validation cohorts. Many previous studies have established multivariate models for predicting ALNM in BC patients based on MRI, some of which have incorporated clinicopathological characteristics (14,21-23,25). Recently, a nomogram based on the ALN status-related factors of the first-stage T1 image of DCE-MRI was constructed to predict ALNM using radiomics (22). The predictive performance of that model was comparable to the radiomics model in this study. Moreover, previous research has constructed nomograms based on the status of three lymph nodes extracted from the peak enhancement period detected by DCE-MRI to predict ALNM, and these nomograms showed promising efficacy in both the training and testing sets (23). A previous study showed that a prediction model based on radiomics features from DCE-MRI had a significantly increased AUC value after correcting for some clinicopathological characteristics (25). Previous research has shown that combining MG with DCE-MRI enhanced the ability of a model to distinguish between benign and malignant BC, and reported that this model had a prediction accuracy of 83.3% (35). In addition, the deep learning approach has also been applied to predict ALNM in BC. This study integrated clinicopathological characteristics, MRI radiomics, and a MG deep learning model to improve the prediction ability.

Our study had some limitations. First, it should be noted that our study was a single-center retrospective study. The patients included are those with upgraded DCIS. These patients often present with palpable mass-type lesions, which are considered as breast malignant lesions. MRI examination is recommended. However, MRI is not a routine examination for the patients with DCIS, which differs from the situation in Europe and the United States. Thus, while all the participants met the inclusion and exclusion criteria, selection bias could not be completely avoided. Limitations include reliance on pre-therapy MRI and uncertain clinical utility in guideline-defined low-risk subgroups.Second, there were minor differences between the two cohorts, which might reduce the reliability of validation. Multi-center, large cohort studies should be conducted in the future. Manual ROI segmentation introduces subjectivity, though reproducibility tests demonstrated acceptable consistency. Future studies may benefit from automated segmentation tools to reduce variability.

Conclusions

In this study, a multi-omics model based on clinicopathological characteristics, MRI radiomics, and MG deep learning was constructed, which showed promising performance in predicting ALNM in patients with upgraded DCIS. The model developed in this study has potential clinical predictive value and might help surgeons to make better clinical decisions. It may help predict additional nodal metastasis in patients who have neo-adjuvant chemotherapy for invasive cancer and undergo a sentinel node with 1 + node, or predict additional + nodes with this approach and other situations where it would be helpful to know the nodal burden without surgical intervention.

Acknowledgments

We extend our sincere gratitude to Y.C. and W.L. for their invaluable contributions to tumor segmentation.

Footnote

Reporting Checklist: The authors have completed the TRIPOD reporting checklist. Available at https://gs.amegroups.com/article/view/10.21037/gs-2025-89/rc

Data Sharing Statement: Available at https://gs.amegroups.com/article/view/10.21037/gs-2025-89/dss

Peer Review File: Available at https://gs.amegroups.com/article/view/10.21037/gs-2025-89/prf

Funding: This study was supported by grants from the National Natural Science Foundation of China (No. 82171898), the Deng Feng Project of High-Level Hospital Construction (No. DFJHBF202109), the Guangdong Basic and Applied Basic Research Foundation (Nos. 2022A1515012277 and 2023A1515010222), the Guangzhou Science and Technology Project (No. 202002030236), the Macao Science and Technology Development Fund (No. 0021070118131610 6/AKP), the Beijing Medical Award Foundation (No. YXJL-2020-0941-0758), the Beijing Science and Technology Innovation Medical Development Foundation (No. KC2022-ZZ-0091-5), the Development Cancer for Medical Science and Technology National Health Commission of the People's Republic of China (No. WKZX2023CX110002), and the Beijing Life Oasis Public Service Center (No. cphcf-2022-058). The funding providers were not involved in the study design, data collection, analysis and interpretation, writing of the report, or the decision to submit the article for publication.

Conflicts of Interest: All authors have completed the ICMJE uniform disclosure form (available at https://gs.amegroups.com/article/view/10.21037/gs-2025-89/coif). The authors have no conflicts of interest to declare.

Ethical Statement: The authors are accountable for all aspects of the work in ensuring that questions related to the accuracy or integrity of any part of the work are appropriately investigated and resolved. The Ethics Committee of the Guangdong Provincial People's Hospital approved this study (No. KY-Q-2022-452-01; date: December 6, 2022) The study was conducted in accordance with the Declaration of Helsinki and its subsequent amendments. The requirement of informed consent was waived due to the retrospective nature of this study.

References

1. Meurs CJC, van Rosmalen J, Menke-Pluijmers MBE, et al. A prediction model for underestimation of invasive breast cancer after a biopsy diagnosis of ductal carcinoma in situ: based on 2892 biopsies and 589 invasive cancers. Br J Cancer 2018;119:1155-62.
2. Kim J, Han W, Lee JW, et al. Factors associated with upstaging from ductal carcinoma in situ following core needle biopsy to invasive cancer in subsequent surgical excision. Breast 2012;21:641-5.
3. Jakub JW, Murphy BL, Gonzalez AB, et al. A Validated Nomogram to Predict Upstaging of Ductal Carcinoma in Situ to Invasive Disease. Ann Surg Oncol 2017;24:2915-24.
4. Brennan ME, Turner RM, Ciatto S, et al. Ductal carcinoma in situ at core-needle biopsy: meta-analysis of underestimation and predictors of invasive breast cancer. Radiology 2011;260:119-28.
5. Goyal A, Douglas-Jones A, Monypenny I, et al. Is there a role of sentinel lymph node biopsy in ductal carcinoma in situ?: analysis of 587 cases. Breast Cancer Res Treat 2006;98:311-4.
6. Doyle B, Al-Mudhaffer M, Kennedy MM, et al. Sentinel lymph node biopsy in patients with a needle core biopsy diagnosis of ductal carcinoma in situ: is it justified? J Clin Pathol 2009;62:534-8.
7. Renshaw AA. Predicting invasion in the excision specimen from breast core needle biopsy specimens with only ductal carcinoma in situ. Arch Pathol Lab Med 2002;126:39-41.
8. Dillon MF, McDermott EW, Quinn CM, et al. Predictors

of invasive disease in breast cancer when core biopsy demonstrates DCIS only. J Surg Oncol 2006;93:559-63.
9. Kurniawan ED, Rose A, Mou A, et al. Risk factors for invasive breast cancer when core needle biopsy shows ductal carcinoma in situ. Arch Surg 2010;145:1098-104.
10. Park HS, Kim HY, Park S, et al. A nomogram for predicting underestimation of invasiveness in ductal carcinoma in situ diagnosed by preoperative needle biopsy. Breast 2013;22:869-73.
11. Park HS, Park S, Cho J, et al. Risk predictors of underestimation and the need for sentinel node biopsy in patients diagnosed with ductal carcinoma in situ by preoperative needle biopsy. J Surg Oncol 2013;107:388-92.
12. Lee CW, Wu HK, Lai HW, et al. Preoperative clinicopathologic factors and breast magnetic resonance imaging features can predict ductal carcinoma in situ with invasive components. Eur J Radiol 2016;85:780-9.
13. Mayerhoefer ME, Materka A, Langs G, et al. Introduction to Radiomics. J Nucl Med 2020;61:488-95.
14. Dong Y, Feng Q, Yang W, et al. Preoperative prediction of sentinel lymph node metastasis in breast cancer based on radiomics of T2-weighted fat-suppression and diffusion-weighted MRI. Eur Radiol 2018;28:582-91.
15. Yang J, Wang T, Yang L, et al. Preoperative Prediction of Axillary Lymph Node Metastasis in Breast Cancer Using Mammography-Based Radiomics Method. Sci Rep 2019;9:4429.
16. Qiu X, Jiang Y, Zhao Q, et al. Could Ultrasound-Based Radiomics Noninvasively Predict Axillary Lymph Node Metastasis in Breast Cancer? J Ultrasound Med 2020;39:1897-905.
17. Song BI. A machine learning-based radiomics model for the prediction of axillary lymph-node metastasis in breast cancer. Breast Cancer 2021;28:664-71.
18. Yang C, Dong J, Liu Z, et al. Prediction of Metastasis in the Axillary Lymph Nodes of Patients With Breast Cancer: A Radiomics Method Based on Contrast-Enhanced Computed Tomography. Front Oncol 2021;11:726240.
19. Jackson VP. Diagnostic mammography. Radiol Clin North Am 2004;42:853-70, vi.
20. Chai R, Ma H, Xu M, et al. Differentiating axillary lymph node metastasis in invasive breast cancer patients: A comparison of radiomic signatures from multiparametric breast MR sequences. J Magn Reson Imaging 2019;50:1125-32.
21. Cui X, Wang N, Zhao Y, et al. Preoperative Prediction of Axillary Lymph Node Metastasis in Breast Cancer using Radiomics Features of DCE-MRI. Sci Rep 2019;9:2240.
22. Han L, Zhu Y, Liu Z, et al. Radiomic nomogram for prediction of axillary lymph node metastasis in breast cancer. Eur Radiol 2019;29:3820-9.
23. Mao N, Dai Y, Lin F, et al. Radiomics Nomogram of DCE-MRI for the Prediction of Axillary Lymph Node Metastasis in Breast Cancer. Front Oncol 2020;10:541849.
24. Narayan AK, Lee CI, Lehman CD. Screening for Breast Cancer. Med Clin North Am 2020;104:1007-21.
25. Song D, Yang F, Zhang Y, et al. Dynamic contrast-enhanced MRI radiomics nomogram for predicting axillary lymph node metastasis in breast cancer. Cancer Imaging 2022;22:17.
26. Zhan C, Hu Y, Wang X, et al. Prediction of Axillary Lymph Node Metastasis in Breast Cancer using Intra-peritumoral Textural Transition Analysis based on Dynamic Contrast-enhanced Magnetic Resonance Imaging. Acad Radiol 2022;29 Suppl 1:S107-15.
27. Abdel-Razeq H, Iweir S, Abdel-Razeq R, et al. Differences in clinicopathological characteristics, treatment, and survival outcomes between older and younger breast cancer patients. Sci Rep 2021;11:14340.
28. Capdet J, Martel P, Charitansky H, et al. Factors predicting the sentinel node metastases in T1 breast cancer tumor: an analysis of 1416 cases. Eur J Surg Oncol 2009;35:1245-9.
29. Lee JH, Kim SH, Suh YJ, et al. Predictors of axillary lymph node metastases (ALNM) in a Korean population with T1-2 breast carcinoma: triple negative breast cancer has a high incidence of ALNM irrespective of the tumor size. Cancer Res Treat 2010;42:30-6.
30. Holm-Rasmussen EV, Jensen MB, Balslev E, et al. Reduced risk of axillary lymphatic spread in triple-negative breast cancer. Breast Cancer Res Treat 2015;149:229-36.
31. Sandoughdaran S, Malekzadeh M, Mohammad Esmaeil ME. Frequency and Predictors of Axillary Lymph Node Metastases in Iranian Women with Early Breast Cancer. Asian Pac J Cancer Prev 2018;19:1617-20.
32. Yoshihara E, Smeets A, Laenen A, et al. Predictors of axillary lymph node metastases in early breast cancer and their applicability in clinical practice. Breast 2013;22:357-61.
33. de la Haba J, Gómez A, Dueñas R, et al. The quotient of number of nodes and tumour size (N/T) from primary breast cancer predicts the clinical course after diagnosis of distant relapse. Eur J Surg Oncol 2004;30:346-51.
34. Liang Y, Benakanakere I, Besch-Williford C, et al.

Synthetic progestins induce growth and metastasis of BT-474 human breast cancer xenografts in nude mice. Menopause 2010;17:1040-7.
35. Zhao YF, Chen Z, Zhang Y, et al. Diagnosis of Breast Cancer Using Radiomics Models Built Based on Dynamic Contrast Enhanced MRI Combined With Mammography. Front Oncol 2021;11:774248.

Cite this article as: Cheng MY, Wu CG, Lin YY, Zou JC, Wang DQ, Haffty BG, Wang K. Development and validation of a multivariable risk model based on clinicopathological characteristics, mammography, and MRI imaging features for predicting axillary lymph node metastasis in patients with upgraded ductal carcinoma *in situ*. Gland Surg 2025;14(4):738-753. doi: 10.21037/gs-2025-89